Earth and Planetary Science Letters 441 (2016) 200–210

Contents lists available at ScienceDirect

Earth and Planetary Science Letters

www.elsevier.com/locate/epsl

Does subduction-induced mantle flow drive backarc extension?

Zhihao Chen *, Wouter P. Schellart, Vincent Strak, João C. Duarte [1]

School of Earth, Atmosphere and Environment, Monash University, Melbourne, VIC 3800, Australia

ARTICLE INFO

Article history:
Received 10 September 2015
Received in revised form 5 February 2016
Accepted 12 February 2016
Available online 4 March 2016
Editor: J. Brodholt

Keywords:
subduction
geodynamic analogue modelling
subduction-induced mantle flow
backarc extension
velocity gradient
shear traction

ABSTRACT

Backarc extension is a characteristic feature of many narrow subduction zones. Seismological and geochemical studies imply the occurrence of mantle flow around the narrow subducting slabs. Previous 3D models suggested that backarc extension is related to subduction-induced toroidal mantle flow. The physical viability of this mechanism, however, has never been tested using laboratory-based geodynamic models. In this work, we present dynamic laboratory models of progressive subduction in three-dimensional (3D) space that were carried out to test this mechanism. To achieve this, we have used a stereoscopic Particle Image Velocimetry (sPIV) technique to map simultaneously overriding plate deformation and 3D subduction-induced mantle flow underneath and around an overriding plate. The results show that the strain field of the overriding plate is characterized by the localization of an area of maximum extension within its interior (at 300–500 km from the trench). The position of maximum extension closely coincides (within ~2 cm, scaling to 100 km) with that of the maximum trench-normal horizontal mantle velocity and velocity gradient measured at a scaled depth of 15–25 km below the base of the overriding plate, and the maximum horizontal gradient of the vertical mantle velocity gradient. We propound that in narrow subduction zones backarc extension in the overriding plate is mainly a consequence of the trench-normal horizontal gradients of basal drag force at the base of the overriding plate. Such shear force gradients result from a horizontal gradient in velocity in the mantle below the base of the lithosphere induced by slab rollback. Calculations based on our models indicate a tensional horizontal trench-normal deviatoric stress in the backarc region scaling to ~28.8 MPa, while the overriding plate trench-normal stress resulting from the horizontal component of the trench suction force is about an order of magnitude smaller, scaling to ~2.4–3.6 MPa.

1. Introduction

During progressive subduction overriding plates may follow the trench and/or deform internally. Such deformation can involve extension or shortening, or the overriding plate may remain undeformed (neutral). Overriding plate deformation is often characterized by backarc extension, which gives rise to backarc basins (Jarrard, 1986; Dvorkin et al., 1993; Heuret and Lallemand, 2005; Schellart, 2008b). For instance, the Aegean and Tyrrhenian Seas are the backarc basins of the Hellenic and Calabria subduction zones, respectively. Structural geological and geophysical investigations have shown that these backarc basins have experienced extension during the Cenozoic (Angelier et al., 1982; Lister et al., 1984; Lonergan and White, 1997; Nicolosi et al., 2006), while seismological and geodetic investigations indicate that they are actively extending today (Amato and Montone, 1997; Kahle et al., 2000; D'Agostino and Selvaggi, 2004; Hollenstein et al., 2008).

Plates and the sub-lithospheric mantle are part of one convective system (Elsasser, 1971; Bercovici, 2003). More than forty years ago it was already suggested that subducted slabs are the dominant driving force of this convective system (Elsasser, 1971). Elsasser (1971), and later Shemenda (1993), further proposed that backarc basins directly result from this subduction process due to trench suction (the force perpendicular to the subduction zone interface) induced by slab rollback. Some authors, however, have argued that backarc basins form due to overriding plate collapse resulting from an excess in potential energy (Hatzfeld et al., 1997; Gautier et al., 1999), while other authors suggested that there is a correspondence between backarc extension and subduction-induced mantle flow below the overriding plate, either in a poloidal fashion (Sleep and Toksöz, 1971) or toroidal fashion (Schellart and Moresi, 2013; Meyer and Schellart, 2013; Duarte et al., 2013; Sternai et al., 2014). Despite the abundant attempts to explain the origin of backarc extension, the fundamental driving mechanism is still a matter of debate.

* Corresponding author. Tel.: +61 03 99024207.
E-mail address: zhihao.chen@monash.edu (Z. Chen).
[1] Now at Instituto Dom Luiz and Geology Department, University of Lisbon, Campo Grande, Lisbon, Portugal.

http://dx.doi.org/10.1016/j.epsl.2016.02.027
0012-821X/

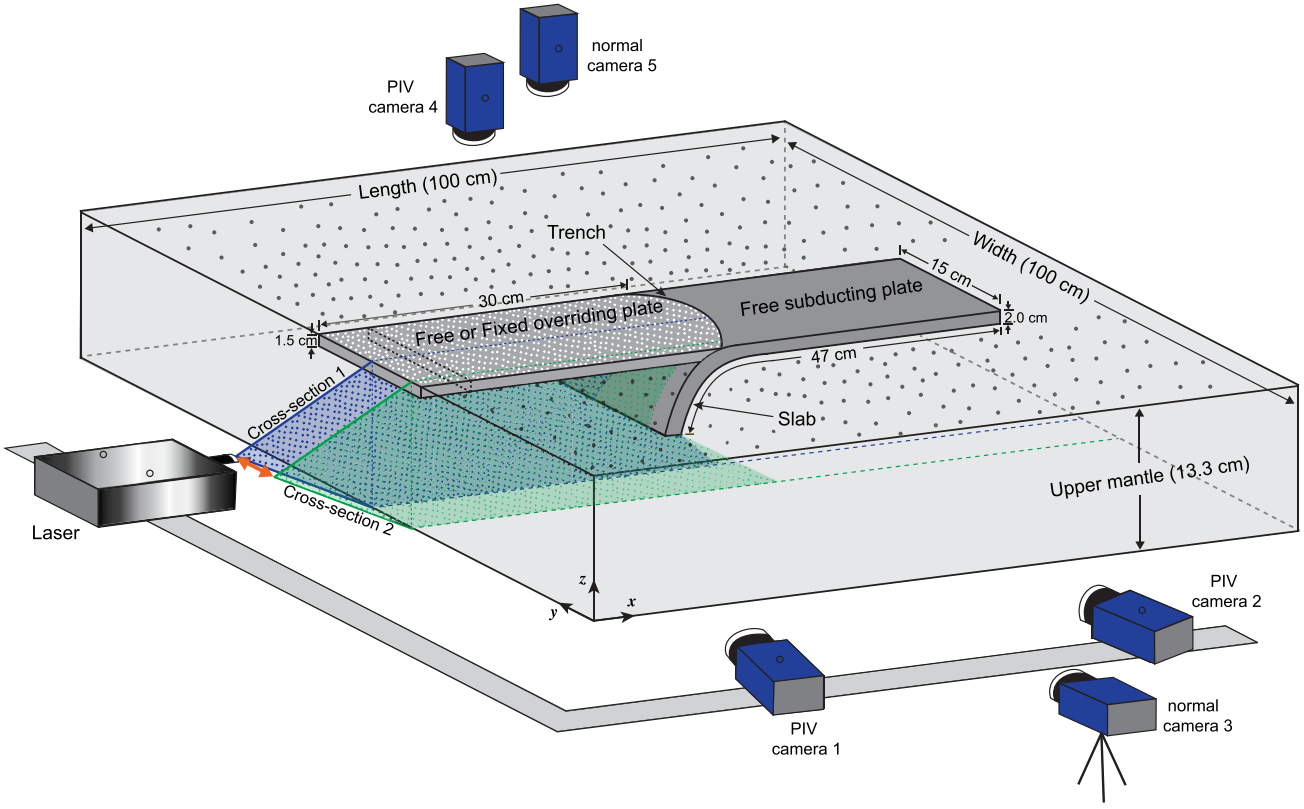

Fig. 1. 3D configuration of the model setup. This setup of subduction includes a free high-viscosity subducting plate, a free/fixed high-viscosity overriding plate, a low-viscosity sub-lithospheric upper mantle and a weak interplate mechanical coupling. The PIV system consists of a laser and three PIV high-resolution cameras. One PIV camera was located above the tank to map the progressive deformation of the overriding plate and mantle flow at the surface, and two PIV cameras were located to the side to map the progressive mantle flow simultaneously in stereo. Two normal cameras (one above and another to the side) were used to record the subduction process. The blue and green dashed lines on the overriding plate indicate the locations of cross-section 1 and cross-section 2, respectively. (For interpretation of the references to color in this figure legend, the reader is referred to the web version of this article.)

Results from seismological and geochemical investigations imply the existence of a 3D subduction-induced mantle flow around lateral slab edges from the subslab zone towards the mantle wedge (Civello and Margheriti, 2004; Zandt and Humphreys, 2008; Hoernle et al., 2008; Long and Silver, 2008; Diaz et al., 2010). Such flow has also been observed in laboratory experiments (Buttles and Olson, 1998; Kincaid and Griffiths, 2003; Schellart, 2004; Funiciello et al., 2004; Schellart, 2008a; Druken et al., 2011; Strak and Schellart, 2014; MacDougall et al., 2014) and numerical models of subduction (Piromallo et al., 2006; Stegman et al., 2006; Schellart et al., 2007; Jadamec and Billen, 2010; Li and Ribe, 2012; Faccenda and Capitanio, 2012; Schellart and Moresi, 2013; Li et al., 2014). It has been previously proposed that this subduction-induced mantle flow is responsible for backarc extension (Schellart and Moresi, 2013; Duarte et al., 2013; Sternai et al., 2014). In particular, using geodynamic numerical models of subduction, Schellart and Moresi (2013) presented quantitative results demonstrating that backarc extension at narrow subduction zones is driven by rollback-induced toroidal mantle flow. However, this driving mechanism has not been examined using physical laboratory models of subduction.

In this work we present analogue experiments that for the first time build a direct link between overriding plate deformation and slab rollback-induced mantle flow. We present buoyancy-driven geodynamic models of progressive subduction in 3D space, including a subducting plate, overriding plate, upper mantle reservoir and weak interplate material. A stereoscopic Particle Image Velocimetry (sPIV) technique has been used to simultaneously map the overriding plate deformation and subduction-induced mantle flow below and around the overriding plate. Such a setup allows us to quantitatively examine the correlation between the overriding plate deformation and the subduction-induced mantle flow.

2. Methods

Our models consist of two layers, following the setups of Duarte et al. (2013) and Meyer and Schellart (2013) (Fig. 1). The top layer is made of a linear-viscous high-viscosity silicone mixed with fine iron powder, simulating a subducting plate (negatively buoyant with density $\rho = 1528$ kg/m^3 and dynamic shear viscosity $\eta_{SP} = 6.07 \times 10^4$ Pa s at 20 °C) and an overriding plate (neutrally buoyant with $\rho = 1428$ kg/m^3 and $\eta_{OP} = 6.01 \times 10^4$ Pa s at 20 °C). The lower layer is made of a linear-viscous low-viscosity glucose syrup ($\rho = 1428$ kg/m^3 and $\eta_{UM} = 289$–291 Pa s), which continues down to 13.3 cm depth (scaling to 665 km of the upper mantle in nature; note that 1 cm scales to 50 km in nature). As such, the rigid bottom of the tank represents the upper–lower mantle discontinuity. The thickness of the subducting plate is 2.0 cm (scaling to 100 km) while that of the overriding plate is 1.5 cm (scaling to 75 km). The width of both plates is 15 cm (scaling to 750 km). The density contrast between the subducting plate and the upper mantle is 100 kg/m^3. A homogeneous lubricant mixture of petrolatum and paraffin oil (with a weak viscoplastic rheology and ~0.8–1.5 Pa flow stress at a shear strain rate of 0.01 s^{-1}) is brushed on the top-surface of the subducting plate to obtain a low mechanical coupling at the subduction zone interface, following the procedure described in Duarte et al. (2013). A 1 mm thick layer of this mixture simulates 5 km of weak hydrated sediments and serpentinized oceanic crust in nature. In our experiment the Reynolds number is very low (3.2×10^{-6}–2.1×10^{-5}, maximally). This ensures that in-

ertial forces are negligible and that the experiments are always in a laminar symmetrical flow regime (Schellart, 2008a), which is a requirement.

The tip of the overriding plate has a wedge-shaped geometry at the start of the experiment. Subduction is initiated by manually down bending 5–7 cm of the subducting plate at an angle of 30–45 degrees. After that, we let subduction evolve without any further external interference. The only driving force in our subduction system is the negative buoyancy of the subducted slab, which is resisted by the viscous sub-lithospheric upper mantle, the viscous plates and the viscous stresses at the subduction zone interface. Our models are scaled to nature following Jacoby (1973) and Duarte et al. (2013), who use the general form of Stokes's settling law to scale experiments (subscript e) to natural systems (subscript n):

$$\frac{\Delta\rho_e l_e^2 g_e}{\eta_e \upsilon_e} = \frac{\Delta\rho_n l_n^2 g_n}{\eta_n \upsilon_n} \quad (1)$$

Where $\Delta\rho$ is the density contrast between slab and ambient mantle, l is a length scale, g is the gravitational acceleration, η is the viscosity of the ambient mantle, and v is the sinking velocity of the slab. Furthermore, we choose a length scale such that 1 cm in the experiments represents 50 km in nature ($l_e/l_n = 2.0 \times 10^{-7}$), and a time scale such that 1 s in the experiments scales to 8300 yr in nature. We perform our experiments in the normal field of gravity, such that $g_e = g_n$. Furthermore, we scale density contrasts such that 100 kg/m^3 in the experiments represents 80 kg/m^3 in nature. From this it follows that our viscosity ratio is $\eta_{\text{UM-}e}/\eta_{\text{UM-}n} = 0.9 \times 10^{-18}$) such that 290 Pa s for the sub-lithospheric mantle in the experiments represents $\sim 3.2 \times 10^{20}$ Pa s in nature. From equation (1) it follows that velocities (v_e) in the experiments scale to velocities in nature (v_n), following:

$$v_n = v_e\{(\Delta\rho_n g_n l_n^2 \eta_e)/(\Delta\rho_e g_e l_e^2 \eta_n)\} \quad (2)$$

Therefore, 0.01 mm/s in the experiments represents 0.6 cm/yr in nature. An effective viscosity ratio between subducting plate and ambient mantle of $\sim$200 was used, which is in the range of natural subduction systems as suggested by previous works ($\sim$100–500) (Funiciello et al., 2008; Schellart, 2008a; Ribe, 2010).

Deformation in the overriding plate and flow in the mantle below are monitored simultaneously by a sPIV system following an approach as described in Strak and Schellart (2014). Three high-resolution cameras (PIV cameras with 2000 × 2000 pixels) and a laser are used to monitor flow from the side (cameras 1 and 2) and strain and flow from the top (camera 4) (Fig. 1). Two normal cameras (cameras 3 and 5) are used for side view and top view perspectives, respectively, to record the whole subduction process. White powder with a size of 0.1–0.3 mm is randomly distributed on the top surface of the overriding plate to quantify the strain field with the PIV system during progressive subduction. Passive tracers of fluorescent polymer particles with a size of 20–50 μm are homogeneously mixed within the glucose syrup. During experiments, a quick (5 μs) 2–4 mm thick vertical laser sheet light (wavelength of 532 nm) oriented perpendicular to the trench illuminates the fluorescent polymer particles, allowing the two side PIV cameras to track the evolution of mantle flow induced by subduction and to quantify the 3D velocity field in cross-sections parallel to the x–z plane (see Fig. 1). The two side PIV cameras, oriented obliquely to the laser sheet, are in stereoscopic arrangement, such that the pair of images recorded by the two side cameras simultaneously can be compared by a stereo cross-correlation technique. Thereby, the 3D mantle flow velocity field can be calculated in individual cross-sections. For more detailed technical information of the PIV system and usage of this system in laboratory subduction experiments please see Strak and Schellart (2014). Black passive markers are located on the top surface of the syrup (upper mantle) around the overriding plate to track the mantle flow and white passive markers are placed at the sides of the subducting plate and overriding plate to track plate motions. We map the flow at two cross section positions (Fig. 1) and four laser sheet shots are used per cross-section, such that there is a total of eight shots for each loop, which has a total duration of 48 s.

Subduction-induced mantle flow has been mapped for two cross-sections and at the top surface: (1) A trench-normal cross-section across the centre of the overriding plate (cross-section 1); (2) A trench-normal cross-section, located at 1.5 cm inboard from the lateral edge of the overriding plate (cross-section 2), and (3) A top view of the mantle flow at the surface next to the plates (Fig. 1). We have carried out experiments with both free and fixed overriding plates simulating the two end members of the natural variability, in which the overriding plate region can correspond to a small and relatively mobile plate or be incorporated within a large, relatively immobile plate, respectively. Movies of the experiments are provided in the supplementary material.

3. Results

3.1. Kinematics

During the first stage of all the experiments, the subduction kinematics is characterized by an increase in velocities due to the gradual acceleration of the sinking slab. After this, the slab starts to interact with the bottom discontinuity, resulting in a decrease in velocities (Fig. 2) and draping of the slab over the bottom of the tank for the model with a free overriding plate (Fig. 3) or the formation of a recumbent fold for the model with a fixed overriding plate (Fig. 4). After this transient stage, subduction enters a quasi-steady-state phase with the slab rolling back through the viscous upper mantle while being draped over the basal discontinuity (Figs. 2–4).

3.2. Overriding plate deformation (OPD)

With progressive subduction, the overriding plate experiences deformation that is characterized by the localization of an area of maximum extensional strain within the interior of the plate, located at 6–10 cm (scaling to 300–500 km) from the trench (Figs. 5–6). During the steady-state slab rollback phase, an area with a maximum extensional strain of 2.2% for the model with a free overriding plate and 12% for the model with a fixed overriding plate, forms within the interior of the overriding plate, at a distance from the trench between 2.5 cm (125 km) and 12.5 cm (625 km) (Figs. 5–6). The frontal edge of the overriding plate experiences some shortening (1.2%) for the model with a free overriding plate (Fig. 5) and extension for the model with a fixed overriding plate (Fig. 6). At the end of the experiments the maximum extensional strain within the overriding plate is up to 10.5% and 39%, respectively. During each experiment the area of maximum strain remains approximately unchanged (Figs. 5–6).

3.3. Subduction-induced mantle flow

Figs. 3 and 4 show the evolution of subduction-induced mantle flow for cross-section 1 in the centre of the overriding plate (see Fig. 1 for the position of cross-section 1). During the free sinking phase, the mantle material flows towards the mantle wedge in the upper half of the upper mantle, but in the opposite direction in the lower half (Figs. 3a–3b and 4a–4b). The mantle velocity in the upper half gradually increases trenchwards, and then rapidly decreases as it approaches the top-surface of the slab. Meanwhile, the mantle material adjacent the top surface of the slab flows

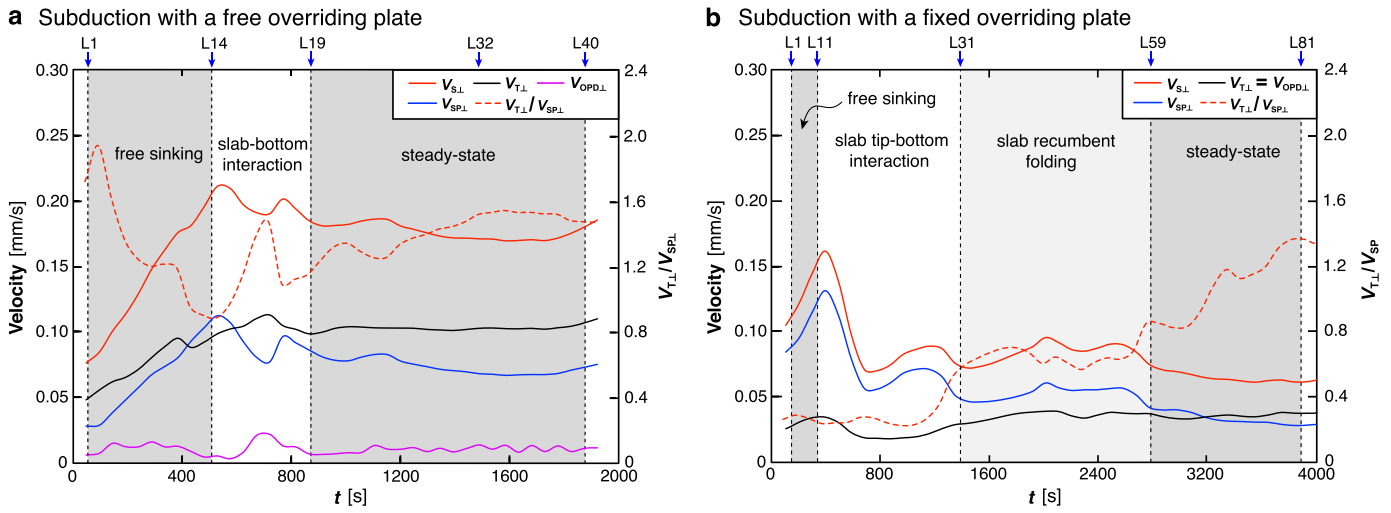

Fig. 2. Kinematics of the subduction models with a free/fixed overriding plate. (**a**) Subduction with a free overriding plate. (**b**) Subduction with a fixed overriding plate. $V_{SP\perp}$ – trench-normal velocity of subducting plate (trenchward is positive); $V_{T\perp}$ – trench-normal velocity of trench (retreat is positive); $V_{OPD\perp}$ – trench-normal velocity of overriding plate deformation (averaged over the entire trench-normal length of the overriding plate, extension is positive); $V_{S\perp}$ – subduction velocity (sum of $V_{SP\perp}$ and $V_{T\perp}$); $V_{T\perp}/V_{SP\perp}$ – ratio of trench-normal trench velocity ($V_{T\perp}$) to trench-normal subducting plate velocity ($V_{SP\perp}$). (For interpretation of the references to color in this figure legend, the reader is referred to the web version of this article.)

down towards the bottom (Figs. 3b and 4b). In the sub-slab region the mantle material moves away towards the subducting plate side (Figs. 3a and 4a). In the steady-state phase, the trenchward mantle flow in the upper half of the upper mantle is more pronounced than in the free sinking phase while the mantle flow in the lower half weakens (Figs. 3c–3d and 4c–4d). The flow pattern of cross-section 2 is very similar to cross-section 1 (Figs. 7b–7c and 8b–8c). Furthermore, the surface flow, calculated from tracking the passive black markers on the top surface of the upper mantle, points to material transport from the sub-slab region around the lateral slab edges towards the mantle wedge region (Figs. 7d and 8d).

3.4. Correlation between OPD and subduction-induced mantle flow

In order to determine the relationship between overriding plate deformation and subduction-induced mantle flow, we quantify and compare both during a late stage of subduction when subduction reaches a steady-state phase (Figs. 7–8). We select this period to calculate their correlation because during this period subduction is characterized by comparable subduction kinematics (trench velocity and subducting plate velocity) (Fig. 2) and comparable mantle flow patterns for both experiments (Figs. 3c–3d and 4c–4d). We quantify the overriding plate finite strain for 22 loops (L19–L40) for the model with a free overriding plate and for 23 loops (L59–L81) for the model with a fixed overriding plate (see Fig. 2 for time lapses). To investigate the relationship between overriding plate strain and subduction-induced mantle flow, the strain is compared with the mantle flow field for three different loops for each model (L19, L32 and L40 for the free overriding plate model and L59, L70 and L81 for the fixed overriding plate model). The results show that the patterns of mantle flow velocity at the three loops for each model are remarkably comparable (Figs. 7e and 8e). Along the trench-normal direction, overriding plate strain progressively increases, from 2.4% at 30 cm (1500 km) from the trench to 5.3% at 12 cm (600 km) from the trench for the free overriding plate model (Fig. 7e) and from 1.9% at 40 cm (2000 km) from the trench to 10.2% at 10 cm (500 km) from the trench for the fixed overriding plate model (Fig. 8e). The horizontal mantle flow velocity (x component) measured at a depth of 0.3–0.5 cm (15–25 km) below the base of the overriding plate also shows a gradual increase, with velocities of 5 mm/min (5 cm/yr) at 30 cm from the trench to 9 mm/min (9 cm/yr) at 12 cm from the trench for the free overriding plate model (Fig. 7e), and with velocities of 0.2–0.3 mm/min (0.2–0.3 cm/yr) at 40 cm from the trench to 2.5 mm/min (2.5 cm/yr) at 10 cm from the trench for the fixed overriding plate model (Fig. 8e). The trench-normal horizontal velocity gradient of mantle flow (dv_x/dx) increases from 0.01–0.02 min^{-1} to 0.025–0.030 min^{-1} (Fig. 7e) and from 0–0.004 min^{-1} to 0.020–0.025 min^{-1} (Fig. 8e), respectively. Furthermore, the trench-normal horizontal gradient of the vertical mantle velocity gradient ($d(dv_x/dz)/dx$) increases from 0.0025–0.005 $mm^{-1}\,min^{-1}$ to 0.00625–0.0075 $mm^{-1}\,min^{-1}$ and from 0–0.001 $mm^{-1}\,min^{-1}$ to 0.005–0.0065 $mm^{-1}\,min^{-1}$. The position of maximum extensional strain of the overriding plate closely coincides with that of the maximum horizontal mantle flow velocity, the maximum horizontal velocity gradient and the maximum horizontal gradient of the vertical mantle velocity gradient (within 0–2 cm (scaling to 0–100 km) from the maximum, please see Figs. 7e and 8e).

4. Discussion

4.1. Conceptual model of backarc extension

Our experimental results show a comparable position of the maximum trench-normal horizontal velocity of mantle flow underneath the plate and the maximum trench-normal extensional strain in the overriding plate (within 0–2 cm of each other) (Figs. 7e1 and 8e1). As such, one could argue for a cause and effect relationship between the two parameters. However, it is not the magnitude of the trench-normal horizontal velocity (v_x) that determines the rate and amount of trench-normal extension, it is the magnitude of the gradient of the sub-lithospheric vertical mantle velocity gradient ($d(dv_x/dz)/dx$) that determines it. In our models dv_x/dx in the silicone plate is negligible compared to dv_x/dx in the syrup below the plate, so the location of maxima of dv_x/dx coincide with those of $d(dv_x/dz)/dx$. Furthermore, a maximum in $d(dv_x/dz)/dx$ and dv_x/dx in the syrup correspond with a maximum in strain rate in the overriding plate, and, if the velocity field is steady-state, with the maximum in strain. Thus, the trench-normal deformation of the overriding plate should be related to the trench-normal velocity gradient in the mantle just below the base of the overriding plate during the steady-state subduction phase, when the mantle velocity field is approximately steady-state

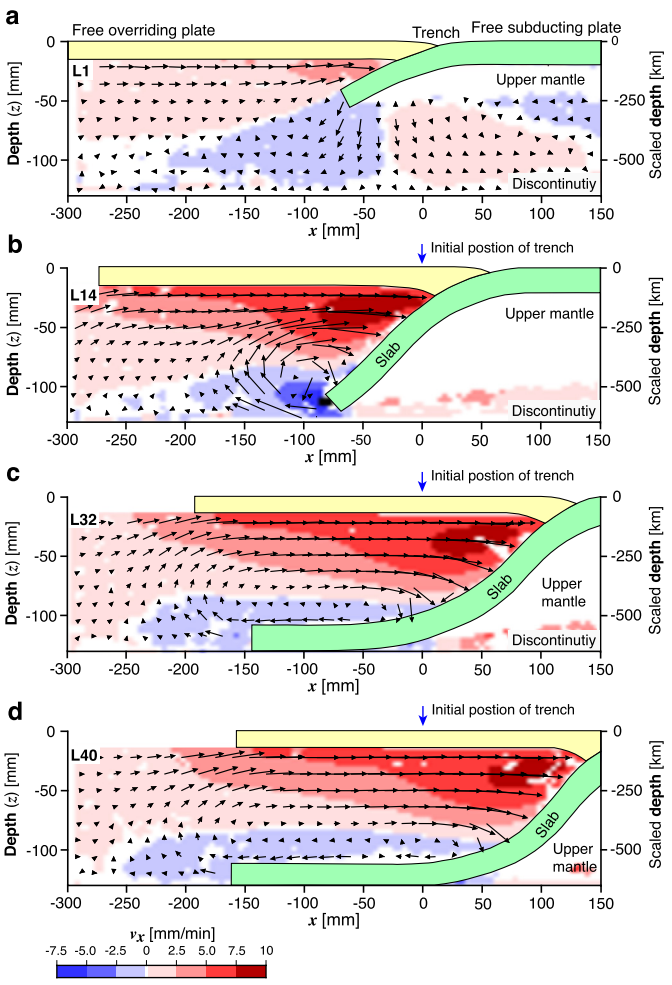

Fig. 3. Evolution of mantle velocity field during progressive subduction for the subduction model with a free overriding plate. (**a**) Mantle flow at L1 (free sinking phase). (**b**) Mantle flow at L14 (slab-discontinuity interaction phase). (**c**) Mantle flow at L32 (steady-state phase). (**d**) Mantle flow at L40 (steady-state phase). Dark and light red (positive) indicate the direction of mantle flow towards the subducting plate side, whereas dark and light blue (negative) indicate the opposite direction of mantle flow. These four profiles of mantle flow are all mapped through the central cross-section (cross-section 1, see Fig. 1 for the positions of cross-sections). Please see Fig. 2a for the time of different loops. (For interpretation of the references to color in this figure legend, the reader is referred to the web version of this article.)

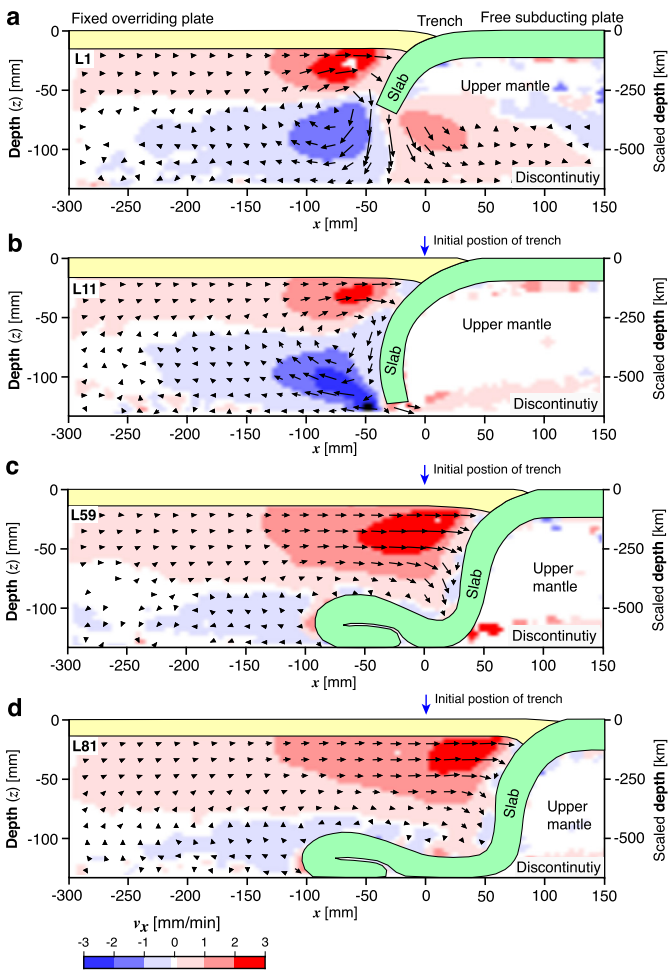

Fig. 4. Evolution of mantle velocity field during progressive subduction for the subduction model with a fixed overriding plate. (**a**) Mantle flow at L1 (free sinking phase). (**b**) Mantle flow at L11 (slab-discontinuity interaction phase). (**c**) Mantle flow at L59 (steady-state phase). (**d**) Mantle flow at L81 (steady-state phase). Dark and light red (positive) indicate the direction of mantle flow towards the subducting plate side, whereas dark and light blue (negative) indicate the opposite direction of mantle flow. These four profiles of mantle flow are all mapped through the central cross-section (cross-section 1, see Fig. 1 for the positions of cross-sections). Please see Fig. 2b for the time of different loops. (For interpretation of the references to color in this figure legend, the reader is referred to the web version of this article.)

as well (compare Figs. 3c and 3d, and compare Figs. 4c and 4d). In our models the positions of the maximum extensional strain and maximum dv_x/dx and $d(dv_x/dz)/dx$ of mantle flow closely coincide and are located within 0–2 cm (scaling to 0–100 km) of each other (Figs. 7–8). The minor offset between some of the velocity gradient profiles can be explained by taking into account the different time lapse for the calculations between the overriding plate strain and the mantle velocity gradient. The period for which the strain map has been calculated is the steady-state slab rollback phase with an interval of thousands of seconds (Fig. 2), while the period for which the mantle velocity field has been calculated is within one loop with an interval of tens of seconds. This difference in time lapses induces a minor offset of maximum extensional strain of the overriding plate towards the trench with respect to the maximum horizontal gradients. The usage of a longer time interval for the strain maps was necessary to properly resolve the strain with the PIV system due to the relatively low strain rates in the experiments.

Our dynamic subduction experiments demonstrate there is a direct link between subduction-induced mantle flow and overriding plate deformation, where rollback-induced toroidal mantle flow creates a trench-normal horizontal velocity gradient below the overriding plate that induces a shear drag gradient at the base of the overriding plate that drives its extension. In our models, the potential energy of the overriding plate plays no role in driving overriding plate extension, because the overriding plate is neutrally buoyant with respect to the underlying sub-lithospheric mantle. In nature, however, most overriding plates are positively buoyant and so the excess potential energy stored in overriding plates will promote extension and collapse towards the subduction zone trench. Our models indicate, however, that such potential energy is not essential for driving overriding plate deformation.

As proposed by earlier investigations, during progressive subduction two types of mantle flow can be produced: one is known as poloidal flow and another known as toroidal flow (Buttles and Olson, 1998; Kincaid and Griffiths, 2003; Schellart, 2004; Funiciello et al., 2004; Stegman et al., 2006; Schellart and Moresi, 2013; Strak and Schellart, 2014). Modelling has shown that the former is caused by downdip movement of the slab and trenchward motion of the subducting plate, and latter is induced by lateral movement of the slab through a viscous mantle, which also causes the trench to migrate (Kincaid and Griffiths, 2003; Schellart, 2004;

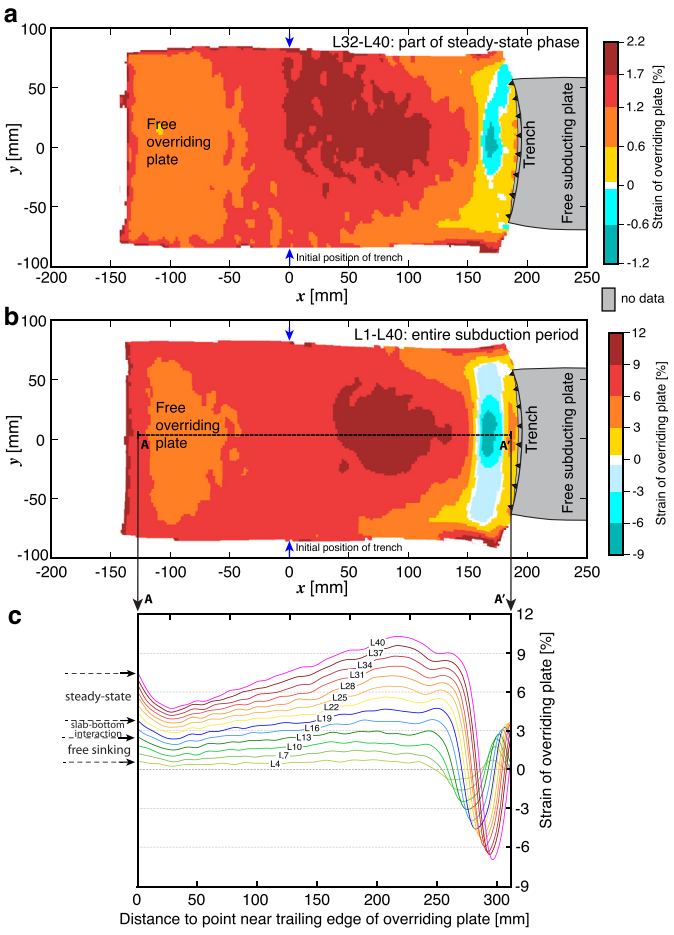

Fig. 5. Trench-normal horizontal normal strain of overriding plate for subduction model with a free overriding plate. (**a**) Part of steady-state slab rollback phase (L32–40), during which the slab is rolling back steadily, as demonstrated by the comparable kinematics of subduction and comparable patterns of mantle flow (see Figs. 2 and 3). Note that this phase in this model is similar as that in the model with a fixed overriding plate in Fig. 6a (between 34.2 cm and 40.8 cm of subduction of the subducting plate, as shown in Fig. 2). (**b**) Total subduction period (L1–L40), which covers the entire duration of the experiment. (**c**) Evolution of strain of overriding plate for the profile (A–A′) across the centre of the overriding plate in b. The strain presented is an accumulated maximum normal strain. In a and b red, orange and yellow (positive) indicate extension, and blue (negative) indicates shortening. The numbers after "L" indicate different loop numbers. The interval time for each loop is constant (48 s). Please see Fig. 2a for the time of different loops. (For interpretation of the references to color in this figure legend, the reader is referred to the web version of this article.)

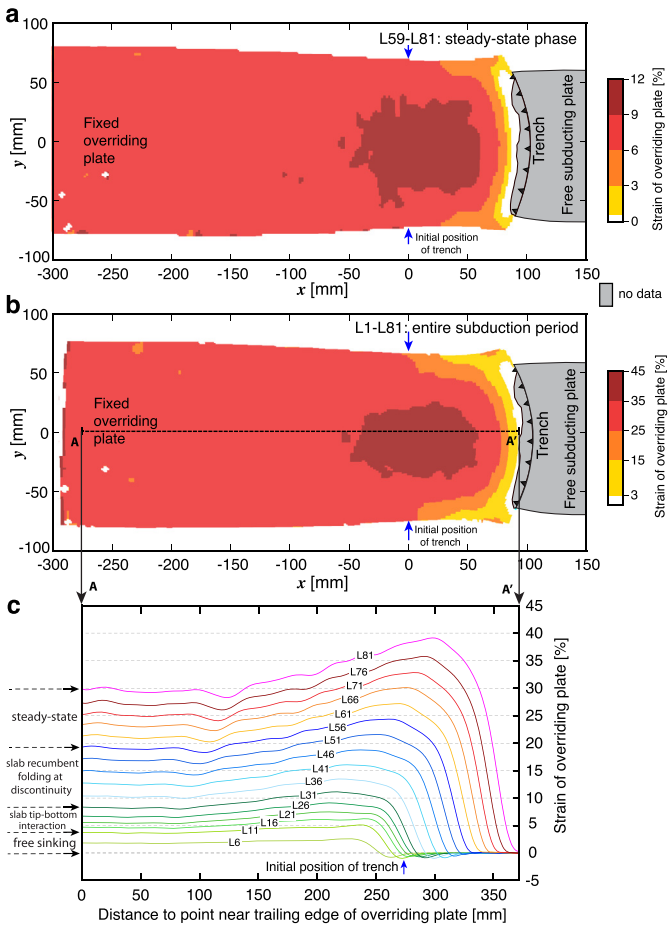

Fig. 6. Trench-normal horizontal normal strain of overriding plate for subduction model with a fixed overriding plate. (**a**) Steady-state slab rollback phase, during which the slab is rolling back steadily, as demonstrated by the comparable kinematics of subduction and comparable patterns of mantle flow (see Figs. 2 and 4). Note that this phase in this model is similar as that in the model with a free overriding plate in Fig. 5a (between 34.2 cm and 40.8 cm of subduction of the subducting plate, as shown in Fig. 2). (**b**) Total subduction period, which covers the entire duration of the experiment. (**c**) Evolution of strain of overriding plate for profile (A–A′) across the middle of the overriding plate. The strain presented is an accumulated maximum normal strain. Red, orange and yellow (positive) in a and b indicate extension. The numbers after "L" indicate different loop numbers. The interval time for each loop is constant (48 s). Please see Fig. 2b for the time of different loops. (For interpretation of the references to color in this figure legend, the reader is referred to the web version of this article.)

Duarte et al., 2013). The two components of subduction-induced mantle flow observed in our experiments are consistent with these previous works. Furthermore, there is an increase of the ratio of trench-normal trench velocity ($V_{T\perp}$) to trench-normal subducting plate velocity ($V_{SP\perp}$) ($V_{T\perp}/V_{SP\perp}$, from 1.2 to 1.5 for the model with a free overriding plate and from 0.8 to 1.8 for the model with a fixed overriding plate, see Fig. 2) at the stage of steady-state slab rollback in our experiments. This indicates that the toroidal component of mantle flow has a relatively higher contribution to overriding plate deformation than the poloidal component, which is consistent with previous experimental results (Schellart and Moresi, 2013; Meyer and Schellart, 2013; Duarte et al., 2013; Chen et al., 2015a).

4.2. Estimating stresses in the overriding plate

In the model with a fixed overriding plate, on inspection of the overriding plate strain field map in Fig. 6, the domain close to trench is nearly neutral with approximately no deformation. This indicates that the horizontal stress components of trench suction and shear at the subduction zone interface have approximate equal magnitudes and opposite signs, such that they cancel each other out. We can thus roughly estimate the stress related to trench suction in our models from quantifying the shear stress at the subduction zone interface. The effective flow stress of the lubrication material filled in the subduction channel of our models is 1.0–1.5 Pa at a strain rate of 0.1 s^{-1} (Duarte et al., 2014). We assume that the thickness of subduction channel in the type of analogue subduction models presented in this study is ~1 mm (Duarte et al., 2013). The average subduction velocity is ~0.08 mm/s (Fig. 2b) and the subduction dip angle is approximately 30 degrees. From this one can calculate that the magnitude of the horizontal component of the shear stress at the subduction zone interface is ~0.6–0.9 Pa, scaling to ~2.4–3.6 MPa in nature, which is also the value of the horizontal component of the trench suction stress. Furthermore, for the model with a fixed overriding plate the maximum total accumulated strain is ~0.45 for the whole subduction process with

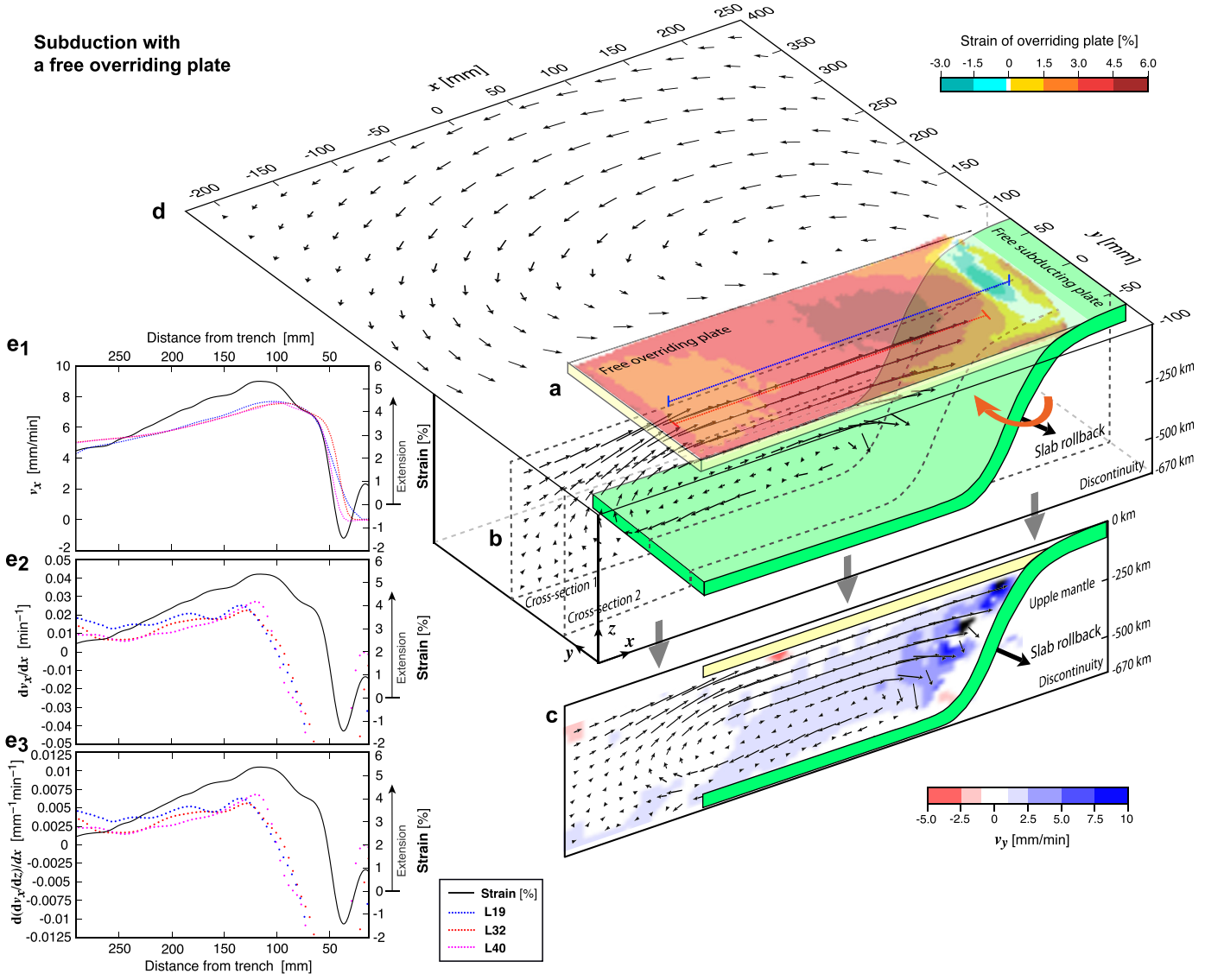

Fig. 7. 3D scheme of overriding plate deformation and mantle flow in the dynamic laboratory model of narrow subduction with a free overriding plate. (**a**) Strain map of overriding plate deformation. Note that the strain is a finite trench-normal maximum normal strain and the strain map was calculated for the steady-state slab rollback stage (L19–L40). Red, orange and yellow (positive) indicate extension, and blue (negative) indicates shortening. (**b**) Velocity field in the central cross-section (cross-section 1, see Fig. 1). (**c**) Velocity field in a cross-section near the lateral edge of the overriding plate and slab, 1.5 cm away from the edge of the overriding plate (cross-section 2, see Fig. 1). Note that the colour scheme indicates mantle flow into (blue) and out of (red) the plane. (**d**) Surface velocity field, which is a top view perspective of mantle flow next to the overriding plate. Note that in b–d the mantle velocity fields were calculated at L40 and the scaling for the size of arrows is comparable. (**e**) Correlation between the strain of the overriding plate and the trench-normal horizontal mantle velocity (v_x), corresponding trench-normal horizontal mantle velocity gradient (dv_x/dx) and trench-normal horizontal gradient of the vertical mantle velocity gradient ($d(dv_x/dz)/dx$) at 3–5 mm (scaling to 15–25 km) below the base of the overriding plate, respectively. The strain curve is a profile across the centre of the overriding plate, the position of which is indicated by a blue line in a. Note that the mantle velocity and velocity gradient profiles were calculated at L19, L32 and L40, the positions of which are indicated by a red line in a. Please see Fig. 2a for the time of different loops. (For interpretation of the references to color in this figure legend, the reader is referred to the web version of this article.)

a duration of 3840 s (80 loops with each loop duration of 48 s), giving a maximum average strain rate of $\sim 1.2 \times 10^{-4}$ s^{-1}. The effective viscosity of the overriding plate is 6.01×10^{-4} s^{-1}. Therefore, the estimated maximum horizontal trench-normal deviatoric stress within the overriding plate is ~7.2 Pa, scaling to 28.8 MPa in nature, which is some 8–12 times larger than the estimated trench suction stress (~0.6–0.9 Pa). This comparison indicates that the trench suction force plays a minor role in driving overriding plate deformation.

In addition, we estimate the force that drives the overriding plate deformation in our subduction models, following the method of Chen et al. (2015a). The scaled overriding plate deformation force we calculated for the model with a fixed overriding plate is $\sim 9.8 \times 10^{12}$ N/m, which is much larger than previous estimates of the ridge push force (~ 2–3×10^{12} N/m) in nature (Parsons and Richter, 1980). This comparison highlights the importance of subduction-induced mantle flow as a driving mechanism for backarc extension.

4.3. Comparison with nature

The model results of a maximum extensional area localized within the interior of the overriding plate are in agreement with observations of narrow subduction zones in nature, which are often characterized by backarc extension. For instance, at the Gibraltar subduction zone the Gibraltar arc has migrated westwards since 30–25 Ma forming an extensional backarc basin (Alboran basin) (Lonergan and White, 1997) and the Calabria subduction

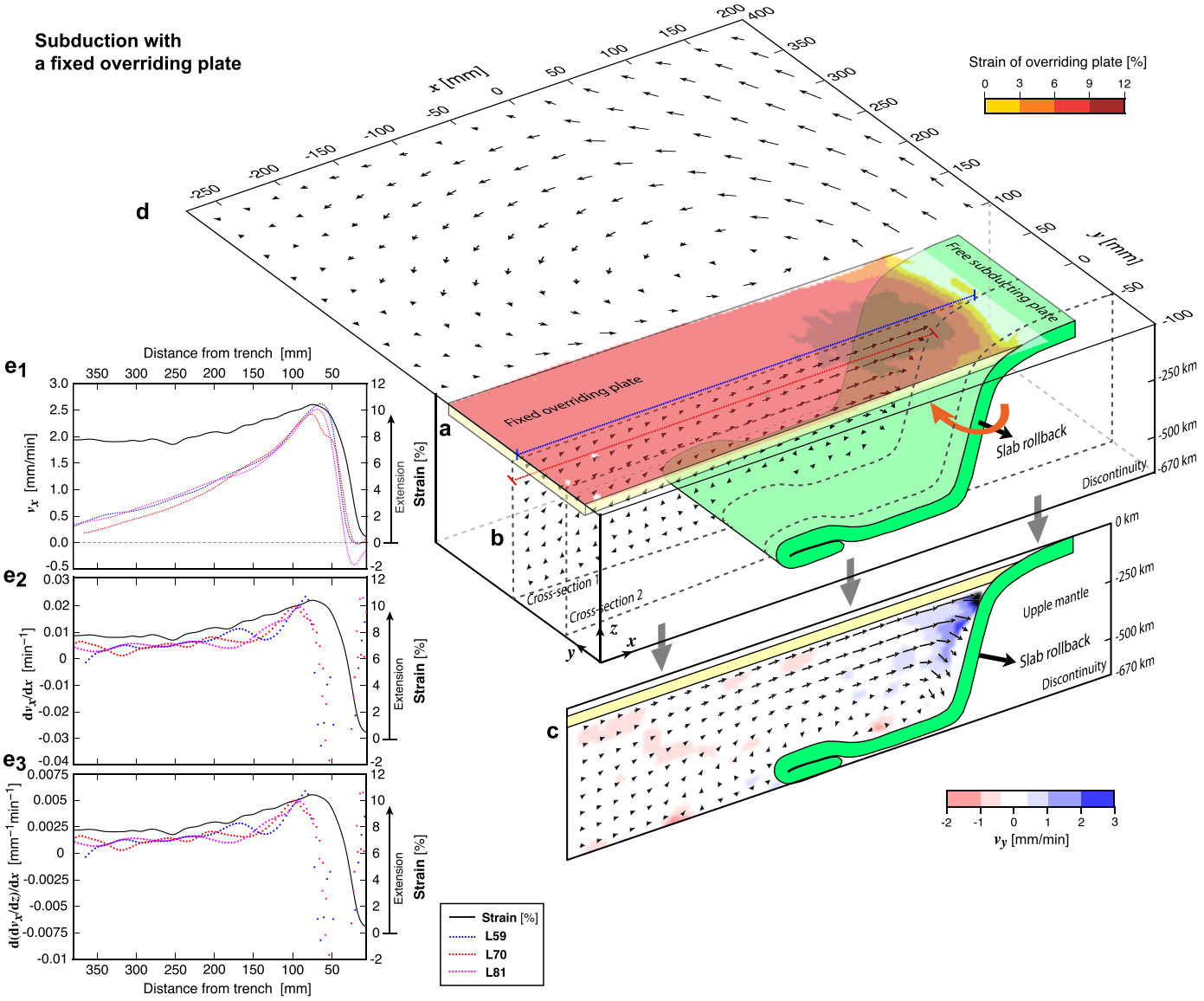

Fig. 8. 3D scheme of overriding plate deformation and mantle flow in the dynamic laboratory model of narrow subduction with a fixed overriding plate. (**a**) Strain map of overriding plate deformation. Note that the strain is a finite trench-normal maximum normal strain and the strain map was calculated for the steady-state slab rollback stage (L59–L81). Red, orange and yellow (positive) indicate extension. (**b**) Velocity field in the central cross-section (cross-section 1, see Fig. 1). (**c**) Velocity field in a cross-section near the lateral edge of the overriding plate and slab, 1.5 cm away from the edge of the overriding plate (cross-section 2, see Fig. 1). Note that the colour scheme indicates mantle flow into (blue) and out of (red) the plane. (**d**) Surface flow, which is a top view perspective of mantle flow next to the overriding plate. Note that in b–d the mantle velocity fields were calculated at L81 and the scaling for the size of arrows is comparable. (**e**) Correlation between the strain of the overriding plate and the trench-normal horizontal mantle velocity (v_x), corresponding trench-normal horizontal mantle velocity gradient (dv_x/dx) and trench-normal horizontal gradient of the vertical mantle velocity gradient ($d(dv_x/dz)/dx$) at 3–5 mm (scaling to 15–25 km) below the base of the overriding plate, respectively. In b–d the mantle velocity fields were calculated at L81. The strain curve is a profile across the centre of the overriding plate, the position of which is indicated by a blue line in a. Furthermore, the mantle velocity and velocity gradient profiles were calculated at L59, L70 and L81, the positions of which are indicated by a red line in a. Please see Fig. 2b for the time of different loops. (For interpretation of the references to color in this figure legend, the reader is referred to the web version of this article.)

zone has migrated SE-ward forming the Tyrrhenian Sea backarc basin (with the Vavilov and Marsili basins) (Malinverno and Ryan, 1986; Jolivet and Faccenna, 2000). Their backarc basins are located at a comparable distance (350–650 km) from the trench as shown in our models (300–500 km). The minor difference in distance could be related to the more complicated rheology (brittle behaviour) and lateral and vertical heterogeneity in strength of tectonic plates in nature while the plates in our models are laterally and vertically homogeneous and consist of linear viscous materials. In addition, results of shear wave splitting measurements around the Gibraltar and Calabria subduction zones imply the existence of subduction-induced toroidal flow around the retreating slab (Civello and Margheriti, 2004; Diaz et al., 2010), the pattern of which is comparable with the toroidal flow observed in our models around the lateral slab edges from the subslab side towards the mantle wedge side (Figs. 7–8). The model results provide direct support that the subduction-induced mantle flow (predominantly toroidal) is responsible for backarc extension. This mechanism can explain backarc extension occurring at narrow subduction zones, such as the Gibraltar and the Calabria subduction zones.

Besides the above two natural prototypes, our model can also provide a mechanism for backarc extension in other narrow subduction zones, such as the Aegean Sea bordering the Hellenic subduction zone (Le Pichon, 1982) and the Scotia Sea bordering the Scotia subduction zone (Livermore, 2003). For the latter subduction zone kinematic studies imply rapid east-directed trench retreat and

slab rollback (Schellart, 2008b), while a shear wave splitting study implies toroidal mantle flow around the lateral slab edges (Müller et al., 2008a). Such rollback-induced toroidal flow could thus drive the extension in the Scotia Sea backarc basin. Figs. 5 and 6 show that the magnitude of extension changes laterally from maximum in the middle and decreasing towards the edges. The most comparable natural prototype is the Scotia backarc basin. Although the ridge spreading rate and the sea-floor age grid are comparable in the direction parallel to the trench (Müller et al., 2008b), the concave shape of the magmatic arc towards backarc basin for the Scotia subduction zone indicates that the magnitude of backarc extension is maximum in the middle, and decreases gradually towards to the edges of the overriding plate.

Even though our models simulate narrow subduction zones (∼750 km), the results can also have a broader application to nature. For wider subduction zones such as the Melanesia subduction system (∼4400 km) and the Northwest Pacific subduction system (∼6550 km), their edge segments (New Britain and New Hebrides segments for the Melanesia, Schellart et al., 2006, and the Mariana segment for the Northwest Pacific, Honza and Fujioka, 2004) are characterized by backarc extension as well. In view of the patterns of mantle flow resulting from slab rollback in our narrow subduction models, we infer that the edges of wider subduction zones are also characterized by the occurrence of toroidal mantle flow driven by the retreating edge segments of wider slabs. Such mantle flow could drive backarc extension at the edge segments of wider subduction zones.

4.4. Comparison with previous modelling studies

With progressive subduction, the onset of slab rollback generates high pressure in the subslab mantle domain (subducting plate side) and low pressure in the mantle wedge (overriding plate side). On the subslab side, the high pressure pushes the mantle material to migrate from the subslab domain around the lateral slab edges towards the mantle wedge in a toroidal fashion (Figs. 3–4 and 7–8), as demonstrated in previous subduction models (Buttles and Olson, 1998; Kincaid and Griffiths, 2003; Schellart, 2004; Funiciello et al., 2004; Piromallo et al., 2006; Stegman et al., 2006; Schellart, 2008a). This type of flow occurs symmetrically at both sides of the slab with one flow cell on either side. These two flow cells diverge in the subslab domain and converge in the mantle wedge domain (Buttles and Olson, 1998; Kincaid and Griffiths, 2003; Schellart, 2004). In the centre of the subduction zone in the mantle wedge domain (symmetry plane where to two toroidal flow cells merge), the mantle velocity is the highest (Kincaid and Griffiths, 2003; Schellart, 2004; Schellart and Moresi, 2013). From our experimental results, we observe that the location of the merging flow cells coincides with the maximum strain area within the overriding plate.

Numerical studies that use a reservoir of sub-lithospheric mantle with a non-Newtonian rheology (Jadamec and Billen, 2012; Jadamec, 2015), as well as rock deformation experiments (Hirth and Kohlstedt, 2003), and observations from shear wave splitting (Long and Wirth, 2013) have suggested a decoupling zone between the sub-lithospheric mantle and the overriding plate close to the subduction zone (<500 km from the trench). The numerical models with a non-Newtonian rheology showed a lateral gradient in the viscosity of the sub-lithospheric mantle, and hence a lateral gradient in upper mantle-overriding plate coupling, characterized by an increasing coupling far from the subduction zone to a region of decreased coupling in the mantle wedge (Jadamec, 2015). This conceptual model has not been directly examined in the current study, but such decoupling is not reproduced in our models, likely because we use linear viscous sub-lithospheric mantle rheologies and isothermal conditions.

In the 3D numerical models presented in Schellart and Moresi (2013), backarc extension dominates for narrow subduction zone settings, comparable to the subduction models presented in the current study. In the 2D numerical models in Schellart and Moresi (2013), extension occurring within the overriding plate is much less pronounced than in the 3D models and only occurs during the initial free sinking phase of the slab. Such 2D subduction models are mostly dominated by overriding plate shortening, which occurs after the initial sinking phase. The shortening can be ascribed entirely to the type of flow in such models, which is strictly poloidal due to the 2D spatial setup. This variation in overriding plate strain with slab rollback rate has been also observed in the 2D numerical models presented in Holt et al. (2015). However, we did not observe this variation in our 3D analogue models of subduction. It is most likely because in 3D subduction models with narrow slabs the overriding plate deformation is dominated by toroidal flow.

Apart from the influence of variation in overriding plate far-field boundary conditions (free vs fixed) on the overriding plate deformation, which is presented in this study and in Chen et al. (2015b), the effect of the variation in other parameters of overriding plate has been examined in previous geodynamic models, such as overriding plate thickness (Meyer and Schellart, 2013; Sharples et al., 2014; Chen et al., 2015a), viscosity ratio between the overriding plate and sub-lithospheric mantle (Chen et al., 2015a) and density (Sharples et al., 2014; Holt et al., 2015). Previous analogue models of subduction showed that when the relative strength of the overriding plate (i.e., the overriding plate thickness and viscosity ratio between the overriding plate and sub-lithospheric mantle) increases, the overriding plate would experience less deformation (Meyer and Schellart, 2013; Chen et al., 2015a). The results from previous 2D numerical models of subduction indicated that when the property of the overriding plate (i.e., thickness and density) is varied, with high buoyancy corresponding to ocean–continent subduction zones and low buoyancy corresponding to ocean–ocean subduction zones, it has significant influence on trench retreat and advance, subduction zone geometry and slab interaction with lower mantle boundary, potentially further impacting on the stress state of the overriding plate (Sharples et al., 2014; Holt et al., 2015).

Previous authors have argued for a dominant role played by trench suction in driving overriding plate extension (e.g., Shemenda, 1993). Following Meyer and Schellart (2013) and Schellart and Moresi (2013), we argue, however, that trench suction is mostly of relevance for affecting forearc deformation. Specifically, the style of forearc deformation (shortening or extension) is influenced by the mobility of the overriding plate through controlling the trench suction normal to the subduction zone interface (Chen et al., 2015b). If the trench suction plays a role in the backarc extension occurring within the overriding plate, shortening would not be produced in the forearc domain. Indeed, the forearc shortening observed in our free overriding plate model indicates that trench suction cannot drive backarc extension located behind the forearc region. Because if trench suction would be the driver of such backarc extension, then the forearc should be experiencing extension as well. In addition, calculations from our experiments indicate that overriding plate stresses resulting from trench suction are some 8–12 times smaller than those resulting from basal drag (see section 4.2).

5. Conclusions

Our 3D fully dynamic analogue models of self-consistent subduction, where the overriding plate deformation and the subduction-induced mantle flow are monitored simultaneously by a stereoscopic PIV system, provide a way to investigate the coupling between lithospheric deformation and flow in the underlying

sub-lithospheric mantle. The experimental results quantitatively support the conceptual model that overriding plate deformation, specifically backarc extension, can be driven by the mantle flow that is induced by progressive subduction. Such subduction-induced mantle flow, in particular the toroidal component, located symmetrically on both sides of the retreating slab, migrates from the sub-slab region around the lateral slab edges towards the mantle wedge region and merges in the central part below the overriding plate. In this central zone the trench-normal velocities, velocity gradients and extensional strain are higher than at the lateral slab edges. Furthermore, the experimental strain is located at 6–10 cm (scaling to 300–500 km) from the trench, which closely coincides with the location of the maximum trench-normal horizontal velocity gradient and the location of the horizontal trench-normal gradient of the vertical mantle velocity gradient in the sub-lithospheric mantle. This gradient causes a maximum trench-normal shear traction gradient at the base of the overriding plate. Our experiments provide a physical basis for the driving mechanism of backarc extension, in which slab rollback-induced toroidal mantle flow drives backarc extension through shear tractions at the base of the overriding plate. We propose that backarc extension in nature is caused in a similar way, and thus predict that those narrow subduction zones that experience (or have recently experienced) backarc extension, are characterized by slab rollback (or recent slab rollback) and toroidal mantle return flow patterns around the lateral slab edges. Furthermore, we estimate the stresses in the overriding plate. Calculations based on our models indicate that the tensional horizontal trench-normal deviatoric stress in the backarc region (scaling to ~28.8 MPa) induced by basal drag is about 8–12 times larger than the trench-normal stress resulting from the horizontal component of the trench suction force (scaling to ~2.4–3.6 MPa).

Acknowledgements

This project was supported by Discovery grants DP110103387 and DP120102983 from the Australian Research Council (ARC) awarded to WPS. ZC was supported by APA and IPRS scholarships from the Australian Government. WPS was supported by a Future Fellowship (FT110100560) from the ARC. JCD is supported by a DECRA fellowship (DF150100326) from the ARC. JCD also acknowledges FCT through project UID/GEO/50019/2013 – Instituto Dom Luiz. We would like to thank Margarete Jadamec and one anonymous reviewer for their constructive comments that significantly improved the manuscript. We also would like to thank the editor John P. Brodholt for handling this manuscript, and we would like to thank Kelin Wang for his constructive comments after initial submission of the manuscript.

Appendix A. Supplementary material

Supplementary material related to this article can be found online at http://dx.doi.org/10.1016/j.epsl.2016.02.027.

References

Amato, A., Montone, P., 1997. Present-day stress field and active tectonics in southern peninsular Italy. Geophys. J. Int. 130, 519–534. http://dx.doi.org/10.1111/j.1365-246X.1997.tb05666.x.

Angelier, J., Lybéris, N., Le Pichon, X., Barrier, E., Huchon, P., 1982. The tectonic development of the Hellenic arc and the Sea of Crete: a synthesis. Tectonophysics 86, 159–196. http://dx.doi.org/10.1016/0040-1951(82)90066-X.

Bercovici, D., 2003. The generation of plate tectonics from mantle convection. Earth Planet. Sci. Lett. 205, 107–121. http://dx.doi.org/10.1016/S0012-821X(02)01009-9.

Buttles, J., Olson, P., 1998. A laboratory model of subduction zone anisotropy. Earth Planet. Sci. Lett. 164, 245–262. http://dx.doi.org/10.1016/S0012-821X(98)00211-8.

Chen, Z., Schellart, W.P., Duarte, J.C., 2015a. Quantifying the energy dissipation of overriding plate deformation in three-dimensional subduction models. J. Geophys. Res., Solid Earth 120, 519–536. http://dx.doi.org/10.1002/2014JB011419.

Chen, Z., Schellart, W.P., Duarte, J.C., 2015b. Overriding plate deformation and variability of fore-arc deformation during subduction: insight from geodynamic models and application to the Calabria subduction zone. Geochem. Geophys. Geosyst. 16, 3697–3715. http://dx.doi.org/10.1002/2015GC005958.

Civello, S., Margheriti, L., 2004. Toroidal mantle flow around the Calabrian slab (Italy) from SKS splitting. Geophys. Res. Lett. 31. http://dx.doi.org/10.1029/2004GL019607.

D'Agostino, N., Selvaggi, G., 2004. Crustal motion along the Eurasia–Nubia plate boundary in the Calabrian Arc and Sicily and active extension in the Messina Straits from GPS measurements. J. Geophys. Res., Solid Earth 109. http://dx.doi.org/10.1029/2004jb002998.

Diaz, J., Gallart, J., Villasenor, A., Mancilla, F., Pazos, A., et al., 2010. Mantle dynamics beneath the Gibraltar Arc (western Mediterranean) from shear-wave splitting measurements on a dense seismic array. Geophys. Res. Lett. 37, L18304. http://dx.doi.org/10.1029/2010GL044201.

Druken, K.A., Long, M.D., Kincaid, C., 2011. Patterns in seismic anisotropy driven by rollback subduction beneath the High Lava Plains. Geophys. Res. Lett. 38, L13310. http://dx.doi.org/10.1029/2011GL047541.

Duarte, J.C., Schellart, W.P., Cruden, A.R., 2013. Three-dimensional dynamic laboratory models of subduction with an overriding plate and variable interplate rheology. Geophys. J. Int. 195, 47–66. http://dx.doi.org/10.1093/Gji/Ggt257.

Duarte, J.C., Schellart, W.P., Cruden, A.R., 2014. Rheology of petrolatum–paraffin oil mixtures: applications to analogue modelling of geological processes. J. Struct. Geol. 63, 1–11. http://dx.doi.org/10.1016/j.jsg.2014.02.004.

Dvorkin, J., Nur, A., Mavko, G., Ben-Avraham, Z., 1993. Narrow subducting slabs and the origin of backarc basins. Tectonophysics 227, 63–79. http://dx.doi.org/10.1016/0040-1951(93)90087-Z.

Elsasser, W.M., 1971. Sea-floor spreading as thermal convection. J. Geophys. Res. 76, 1101–1112. http://dx.doi.org/10.1029/JB076i005p01101.

Faccenda, M., Capitanio, F.A., 2012. Development of mantle seismic anisotropy during subduction-induced 3-D flow. Geophys. Res. Lett. 39, L11305. http://dx.doi.org/10.1029/2012GL051988.

Funiciello, F., Faccenna, C., Giardini, D., 2004. Role of lateral mantle flow in the evolution of subduction systems: insights from laboratory experiments. Geophys. J. Int. 157, 1393–1406. http://dx.doi.org/10.1111/j.1365-246X.2004.02313.x.

Funiciello, F., Faccenna, C., Heuret, A., Lallemand, S., Di Giuseppe, E., et al., 2008. Trench migration, net rotation and slab–mantle coupling. Earth Planet. Sci. Lett. 271, 233–240. http://dx.doi.org/10.1016/j.epsl.2008.04.006.

Gautier, P., Brun, J.-P., Moriceau, R., Sokoutis, D., Martinod, J., et al., 1999. Timing, kinematics and cause of Aegean extension: a scenario based on a comparison with simple analogue experiments. Tectonophysics 315, 31–72. http://dx.doi.org/10.1016/s0040-1951(99)00281-4.

Hatzfeld, D., Martinod, J., Bastet, G., Gautier, P., 1997. An analog experiment for the Aegean to describe the contribution of gravitational potential energy. J. Geophys. Res., Solid Earth 102, 649–659. http://dx.doi.org/10.1029/96jb02594.

Heuret, A., Lallemand, S., 2005. Plate motions, slab dynamics and back-arc deformation. Phys. Earth Planet. Inter. 149, 31–51. http://dx.doi.org/10.1016/j.pepi.2004.08.022.

Hirth, G., Kohlstedt, D., 2003. Rheology of the upper mantle and the mantle wedge: a view from the experimentalists. In: Inside the Subduction Factory, pp. 83–105.

Hoernle, K., Abt, D.L., Fischer, K.M., Nichols, H., Hauff, F., et al., 2008. Arc-parallel flow in the mantle wedge beneath, Costa Rica and Nicaragua. Nature 451, 1094–1097. http://dx.doi.org/10.1038/nature06550.

Hollenstein, C., Müller, M.D., Geiger, A., Kahle, H.G., 2008. Crustal motion and deformation in Greece from a decade of GPS measurements, 1993–2003. Tectonophysics 449, 17–40. http://dx.doi.org/10.1016/j.tecto.2007.12.006.

Holt, A.F., Becker, T.W., Buffett, B.A., 2015. Trench migration and overriding plate stress in dynamic subduction models. Geophys. J. Int. 201, 172–192. http://dx.doi.org/10.1093/gji/ggv011.

Honza, E., Fujioka, K., 2004. Formation of arcs and backarc basins inferred from the tectonic evolution of Southeast Asia since the Late Cretaceous. Tectonophysics 384, 23–53. http://dx.doi.org/10.1016/j.tecto.2004.02.006.

Jacoby, W.R., 1973. Model experiment of plate movements. Nat. Phys. Sci. 242, 130–134. http://dx.doi.org/10.1038/physci242130a0.

Jadamec, M.A., Billen, M.I., 2010. Reconciling surface plate motions with rapid three-dimensional mantle flow around a slab edge. Nature 465, 338–342. http://dx.doi.org/10.1038/nature09053.

Jadamec, M.A., Billen, M.I., 2012. The role of rheology and slab shape on rapid mantle flow: three-dimensional numerical models of the Alaska slab edge. J. Geophys. Res. 117, B02304. http://dx.doi.org/10.1029/2011JB008563.

Jadamec, M.A., 2015. Slab driven mantle weakening and rapid mantle flow. In: Morra, G., Yuen, D.A., King, S., Lee, S., Stein, S. (Eds.), Subduction Dynamics. In: Geophysical Monograph Series, vol. 211, pp. 135–155.

Jarrard, R.D., 1986. Relations among subduction parameters. Rev. Geophys. 24, 217–284. http://dx.doi.org/10.1029/RG024i002p00217.

Jolivet, L., Faccenna, C., 2000. Mediterranean extension and the Africa–Eurasia collision. Tectonics 19, 1095–1106. http://dx.doi.org/10.1029/2000TC900018.

Kahle, H.G., Cocard, M., Peter, Y., Geiger, A., Reilinger, R., et al., 2000. GPS-derived strain rate field within the boundary zones of the Eurasian, African, and Arabian Plates. J. Geophys. Res., Solid Earth 105, 23353–23370. http://dx.doi.org/10.1029/2000jb900238.

Kincaid, C., Griffiths, R.W., 2003. Laboratory models of the thermal evolution of the mantle during rollback subduction. Nature 425, 58–62. http://dx.doi.org/10.1038/nature01923.

Le Pichon, X., 1982. Land-locked oceanic basins and continental collision: the Eastern Mediterranean as a case example. In: Mountain Building Processes, pp. 201–211.

Li, Z.H., Ribe, N.M., 2012. Dynamics of free subduction from 3-D boundary element modeling. J. Geophys. Res., Solid Earth 117, B06408. http://dx.doi.org/10.1029/2012JB009165.

Li, Z.H., Di Leo, J.F., Ribe, N.M., 2014. Subduction-induced mantle flow, finite strain, and seismic anisotropy: numerical modeling. J. Geophys. Res., Solid Earth 119, 5052–5076. http://dx.doi.org/10.1002/2014JB010996.

Lister, G.S., Banga, G., Feenstra, A., 1984. Metamorphic core complexes of Cordilleran type in the Cyclades, Aegean Sea, Greece. Geology 12, 221–225.

Livermore, R.A., 2003. Back-arc spreading and mantle flow in the East Scotia Sea. Geol. Soc. (Lond.) Spec. Publ. 219, 315–331. http://dx.doi.org/10.1144/GSL.SP.2003.219.01.15.

Lonergan, L., White, N., 1997. Origin of the Betic-Rif mountain belt. Tectonics 16, 504–522. http://dx.doi.org/10.1029/96TC03937.

Long, M.D., Silver, P.G., 2008. The subduction zone flow field from seismic anisotropy: a global view. Science 319, 315–318. http://dx.doi.org/10.1126/science.1150809.

Long, M.D., Wirth, E.A., 2013. Mantle flow in subduction systems: the mantle wedge flow field and implication for wedge processes. J. Geophys. Res., Solid Earth 118, 583–606. http://dx.doi.org/10.1002/jgrb.50063.

MacDougall, J.G., Kincaid, C., Szwaja, S., Fischer, K.M., 2014. The impact of slab dip variations, gaps and rollback on mantle wedge flow: insights from fluids experiments. Geophys. J. Int. 197, 705–730. http://dx.doi.org/10.1093/gji/ggu053.

Malinverno, A., Ryan, W.B.F., 1986. Extension in the Tyrrhenian Sea and shortening in the Apennines as result of arc migration driven by sinking of the lithosphere. Tectonics 5, 227–245. http://dx.doi.org/10.1029/TC005i002p00227.

Meyer, C., Schellart, W.P., 2013. Three-dimensional dynamic models of subducting plate-overriding plate—upper mantle interaction. J. Geophys. Res., Solid Earth 118, 775–790. http://dx.doi.org/10.1002/Jgrb.50078.

Müller, C., Bayer, B., Eckstaller, A., Miller, H., 2008a. Mantle flow in the South Sandwich subduction environment from source—side shear wave splitting. Geophys. Res. Lett. 35, L03301. http://dx.doi.org/10.1029/2007GL032411.

Müller, R.D., Sdrolias, M., Gaina, C., Roest, W.R., 2008b. Age, spreading rates, and spreading asymmetry of the world's ocean crust. Geochem. Geophys. Geosyst. 9, Q04006. http://dx.doi.org/10.1029/2007GC001743.

Nicolosi, I., Speranza, F., Chiappini, M., 2006. Ultrafast oceanic spreading of the Marsili Basin, southern Tyrrhenian Sea: evidence from magnetic anomaly analysis. Geology 34, 717–720. http://dx.doi.org/10.1130/G22555.1.

Parsons, B., Richter, F.M., 1980. A relation between the driving force and geoid anomaly associated with mid-ocean ridges. Earth Planet. Sci. Lett. 51, 445–450. http://dx.doi.org/10.1016/0012-821X(80)90223-X.

Piromallo, C., Becker, T.W., Funiciello, F., Faccenna, C., 2006. Three-dimensional instantaneous mantle flow induced by subduction. Geophys. Res. Lett. 33, L08304. http://dx.doi.org/10.1029/2005GL025390.

Ribe, N.M., 2010. Bending mechanics and mode selection in free subduction: a thin-sheet analysis. Geophys. J. Int. 180, 559–576. http://dx.doi.org/10.1111/j.1365-246X.2009.04460.x.

Schellart, W.P., 2004. Kinematics of subduction and subduction-induced flow in the upper mantle. J. Geophys. Res., Solid Earth 109, B07401. http://dx.doi.org/10.1029/2004JB002970.

Schellart, W.P., 2008a. Kinematics and flow patterns in deep mantle and upper mantle subduction models: influence of the mantle depth and slab to mantle viscosity ratio. Geochem. Geophys. Geosyst. 9, Q03014. http://dx.doi.org/10.1130/B26360.1.

Schellart, W.P., 2008b. Overriding plate shortening and extension above subduction zones: a parametric study to explain formation of the Andes Mountains. Geol. Soc. Am. Bull. 120, 1441–1454. http://dx.doi.org/10.1130/B26360.1.

Schellart, W.P., Moresi, L., 2013. A new driving mechanism for backarc extension and backarc shortening through slab sinking induced toroidal and poloidal mantle flow: results from dynamic subduction models with an overriding plate. J. Geophys. Res., Solid Earth 118, 3221–3248. http://dx.doi.org/10.1002/jgrb.5017.

Schellart, W.P., Lister, G.S., Toy, V.G., 2006. A Late Cretaceous and Cenozoic reconstruction of the Southwest Pacific region: tectonics controlled by subduction and slab rollback processes. Earth-Sci. Rev. 76, 191–233. http://dx.doi.org/10.1016/j.earscirev.2006.01.002.

Schellart, W.P., Freeman, J., Stegman, D.R., Moresi, L., May, D., 2007. Evolution and diversity of subduction zones controlled by slab width. Nature 446, 308–311. http://dx.doi.org/10.1038/nature05615.

Sharples, W., Jadamec, M.A., Moresi, L.N., Capitanio, F.A., 2014. Overriding plate controls on subduction evolution. J. Geophys. Res., Solid Earth 119, 6684–6704. http://dx.doi.org/10.1002/2014JB011163.

Shemenda, A.I., 1993. Subduction of the lithosphere and back arc dynamics: insights from physical modeling. J. Geophys. Res., Solid Earth 98, 16167–16185. http://dx.doi.org/10.1029/93JB01094.

Sleep, N., Toksöz, M.N., 1971. Evolution of marginal basins. Nature 233, 548–550. http://dx.doi.org/10.1038/233548a0.

Stegman, D.R., Freeman, J., Schellart, W.P., Moresi, L., May, D., 2006. Influence of trench width on subduction hinge retreat rates in 3-D models of slab rollback. Geochem. Geophys. Geosyst. 7, Q03012. http://dx.doi.org/10.1029/2005GC001056.

Sternai, P., Jolivet, L., Menant, A., Gerya, T., 2014. Driving the upper plate surface deformation by slab rollback and mantle flow. Earth Planet. Sci. Lett. 405, 110–118. http://dx.doi.org/10.1016/j.epsl.2014.08.023.

Strak, V., Schellart, W.P., 2014. Evolution of 3-D subduction-induced mantle flow around lateral slab edges in analogue models of free subduction analysed by stereoscopic particle image velocimetry technique. Earth Planet. Sci. Lett. 403, 368–379. http://dx.doi.org/10.1016/j.epsl.2014.07.007.

Zandt, G., Humphreys, E.D., 2008. Toroidal mantle flow through the western US slab window. Geology 36, 295–298. http://dx.doi.org/10.1130/G24611A.1.